2.

WSRC-TR-91-141

HELIUM BUBBLE DISTRIBUTIONS IN REACTOR TANK REPAIR SPECIMENS - PART I. (U)

by M. H. Tosten, et al.

Westinghouse Savannah River Company
Savannah River Site
Aiken, South Carolina 29808

WSRC-TR--91-141

DE93 003374

P. A. Kestin

DISCLAIMER

This paper was prepared in connection with work done under Contract No. DE-AC09-89SR18035 with the U. S. Department of Energy.

DISCLAIMER

WSRC-TR-91-141

NRTSC
NUCLEAR REACTOR TECHNOLOGY
AND SCIENTIFIC COMPUTATIONS

Keywords:
Electron Microscopy
Reactor Vessel
Stainless Steel
Helium
Bubbles
Welding

Retention - Permanent

HELIUM BUBBLE DISTRIBUTIONS IN REACTOR TANK REPAIR SPECIMENS - PART I. (U)

(By)

M. H. Tosten
P. A. Kestin

ISSUED: MARCH, 1992

D. Thomas Rankin
Derivative Classifier

SRL SAVANNAH RIVER LABORATORY, AIKEN, SC 29808
Westinghouse Savannah River Company
Prepared for the U. S. Department of Energy under Contract DE-AC09-89SR18035

WSRC-TR-91-141

NRTSC
NUCLEAR REACTOR TECHNOLOGY
AND SCIENTIFIC COMPUTATIONS

Keywords:
Electron Microscopy
Reactor Vessel
Stainless Steel
Helium
Bubbles
Welding

Retention - Permanent

HELIUM BUBBLE DISTRIBUTIONS IN REACTOR TANK REPAIR SPECIMENS - PART I. (U)

(By)

M. H. Tosten
P. A. Kestin

ISSUED: MARCH, 1992

D. Thomas Rankin
Derivative Classifier

SRL SAVANNAH RIVER LABORATORY, AIKEN, SC 29808
Westinghouse Savannah River Company
Prepared for the U. S. Department of Energy under Contract DE-AC09-89SR18035

PROJECT: Reactor Repair Program

DOCUMENT: WSRC-TR-91-141

TITLE: HELIUM BUBBLE DISTRIBUTIONS IN REACTOR TANK REPAIR SPECIMENS - PART I. (U)

APPROVALS

S. L. West

S. L. West, TECHNICAL REVIEWER
MATERIALS TECHNOLOGY

DATE: 3/2/92

D. T. Rankin

D. T. Rankin, MANAGER
MATERIALS TECHNOLOGY

DATE: 3/2/92

T. L. Capeletti

T. L. Capeletti, MANAGER
MATERIALS TECHNOLOGY

DATE: 3/2/92

SUMMARY

Transmission electron microscopy (TEM) was employed to characterize the microstructure and helium bubble distributions in Type 304 stainless steel used as substrate material for low heat input gas metal arc (GMA) weld overlays. Helium-free and helium-containing specimens were examined in both the welded and unwelded conditions. The bubble distributions in the helium-bearing plates were characterized according to bubble size, spacing and location within the material. The results of this study showed that a well-developed helium bubble microstructure was present in the test specimens prior to GMA welding. Additionally, the temperature excursion and stresses experienced during (and after) welding did not significantly affect the pre-existing helium bubble distributions at distances 2.3 mm and greater below the weld fusion line.

INTRODUCTION

The Reactor Tank Repair (RTR) program was initiated to develop an in-tank repair process capable of repairing stress corrosion cracks within the SRS reactor tank walls, in the event that such a repair is needed. Previous attempts to repair C-reactor tank with a gas tungsten arc (GTA) welding process were unsuccessful due to significant cracking that occurred in the heat-affected-zones adjacent to the repair welds [1]. It was determined that this additional cracking was a result of helium embrittlement caused by the combined effects of helium (existing within the tank walls), the high heat input associated with the GTA process, and weld shrinkage stresses. Based on the results of earlier studies it was suggested that the effects of helium embrittlement could be minimized by using a low heat input GMA process [2]. Metallographic analysis played an important role throughout the investigation of alternative welding methods for the repair of helium-containing materials [3].

In support of the RTR program, studies were undertaken at the Savannah River Laboratory to systematically examine the effects of the GMA welding process on microstructure and helium bubble distribution in simulated reactor tank material Type 304 stainless steel was chosen as the material most representative of the actual SRS reactor tank walls. Helium was generated within the test specimens through tritium charging and aging, i.e., tritium was allowed to diffuse into the metal lattice where it subsequently

decayed to ^{3}He by the $^{3}H(\beta)^{3}He$ reaction - the "tritium-trick". (Helium, actually ^{4}He, in the reactor tank walls is produced through the $^{10}B(n,\alpha)^{7}Li$ and $^{58}Ni(n,\gamma)^{59}Ni(n,\alpha)^{56}Fe$ reactions.) Due to the fine scale of the helium bubbles present after "tritium-tricking", characterization of the ^{3}He distribution was only possible through the use of transmission electron microscopy. The purpose of this report is to describe the microstructure of the Type 304 stainless steel substrate material and to characterize the helium bubble distributions in specimens containing 147 appm ^{3}He - both with and without a GMA weld overlay.

EXPERIMENTAL PROCEDURE

Type 304 stainless steel plate, received from Sandmeyer Steel Co. in Philadelphia, PA, served as the weld substrate material. The composition of this material is listed in Table 1. The as-received plate was ~12.7 mm (0.5 in.) thick and had been solution annealed at 1040°C and fast cooled in air. Test specimens, measuring ~119 mm (4.7 in.) x ~33 mm (1.3 in.) x ~6 mm (0.25 in.), were cut from this plate. Tritium-charging, aging and offgassing was performed by Sandia National Laboratories in Livermore, CA. Specimens were charged in high-pressure tritium for 30 days at 400°C to produce a uniform distribution throughout the cross section of the plates, and were subsequently aged at -40°C for different lengths of time to generate several target ^{3}He concentrations. Following aging, all specimens were vacuum offgassed at 450°C for 5 days to remove any tritium that remained.

In the present study, TEM was used to examine as-received plate, as-received plate with a GMA overlay, 147 appm ^{3}He plate (no weld), and 147 appm ^{3}He plate with a GMA overlay. (The heat input for the GMA weld overlays was approximately 25.6 kJ/in.^{2}) Specimens for TEM were 3 mm (0.12 in.) disks punched from thin slices of the substrate material. Slices from the welded plates were made parallel to the fusion line at selected locations below the weld overlays (Figure 1). TEM specimens from the as-received plate (no weld) and 147 appm ^{3}He (no weld) plate were taken at random orientations from the bulk material.

Specimen disks were ground to ~0.1 mm (0.004 in.) in thickness and polished to perforation with a twin-jet electropolisher. The

electrolytic solution employed consisted of 7 vol% perchloric acid, 36 vol% butylcellosolve and 57 vol% methanol. Polishing was accomplished by using an applied potential of 12V with the solution cooled to approximately -10°C. After thinning, the foils were rinsed for 1 minute in a steady stream of ethanol. All specimens were examined in a Philips EM400T operating at 120 kV.

Helium bubbles were imaged with a technique that required viewing (and photographing) the specimen in an out-of-focused condition [4]. Using this technique, bubbles imaged in an under-focused condition are bright while those viewed in an over-focused condition are dark. The resolution of this imaging technique is approximately 0.8 nm. Bubbles smaller than this size are not visible due to their lack of contrast above background levels. Most of the micrographs presented in this report were taken in the under-focused condition where the bubbles appear as small "voids" in the material.

Helium bubble distributions were analyzed by measuring bubble size and spacing along grain boundaries and within the grain volumes. These measurements were taken directly from TEM plates or photographic prints. Bubble size was measured from under-focused images where the diameter of the inner bright area of each bubble image was taken as its actual diameter [4]. Since no attempt was made to account for specimen tilt or foil thickness, bubble spacing measurements that were made in this study are relatively inaccurate and are used for comparative purposes only.

RESULTS AND DISCUSSION

As-received Plate

The microstructure of the as-received plate consisted predominantly of recrystallized grains ranging from 20 to 100 μm in diameter. Many of these grains contained annealing twins. In general, the dislocation density in most regions was typical of solution annealed material; however, in some areas very high dislocation densities were observed. Selected area electron diffraction analysis of these regions revealed them to be either heavily cold-worked austenite or areas of α-martensite.

Carbides ($M_{23}C_6$) were present throughout the material on the grain boundaries as well as on incoherent twin boundaries. The latter observation is illustrated in Figures 2a and b. Figure 2a is a bright field micrograph of a region containing an annealing twin boundary. The long, straight portions of this boundary are the coherent boundary segments and the small "steps" are the incoherent segments. Incoherent twin boundaries are preferential sites for carbide precipitation and, although not particularly obvious in this micrograph, each one of the "steps" was decorated with carbides. This observation is better evidenced in Figure 2b, a centered-dark field image from the same region as 2a. In this micrograph only electrons diffracted from the lattice planes of the carbides have contributed to the image. Analysis of higher magnification images from this area indicated that the carbides were approximately 10 nm in diameter.

As-received Plate With GMA Overlay

The as-received plate with a weld overlay was sectioned to reveal the microstructure at 1 and 3 mm below the weld. The microstructure 3 mm below the overlay was characterized by planar dislocation arrays (Figure 3) and pile-ups at the grain boundaries (Figure 4). The dislocation density at this distance from the weld was very low and was representative of material having experienced very limited plastic strain. The microstructure at 1 mm below the weld (Figures 5 and 6) showed an increase in dislocation density over that observed at 3 mm. The amount of plastic strain in this region was estimated to be 2-3%. In general, dislocations were restricted to planar arrays but, infrequently, areas of dislocation tangles were observed (Figure 6). The higher temperatures experienced at this distance from the weld most probably led to dislocation climb and the subsequent loss of the planar arrays in some areas. It should also be mentioned that carbides were not observed in the regions examined at either 1 or 3 mm from the weld.

Helium-bearing Plate (147 appm He, 3.5 mm Below Overlay)

The base microstructure of the helium-bearing material was very similar to the helium-free material except that carbides were observed on the grain boundaries and incoherent twin boundaries. Dislocation densities observed at this distance from the weld were comparable to those found in the as-received material.

formed on the {111} austenite planes. Figure 11 illustrates a typical dislocation loop distribution. In this micrograph, the matrix beam direction is ~[110] and, as such, two sets of {111} planes are upright in the foil. As a result, two variants of the dislocation loops are viewed edge-on in this foil orientation. Several of these loops have been arrowed, A, in this image. The remainder of the loops lie on the other two sets of {111} planes inclined at ~35° to the electron beam. Close examination of Figure 11 also shows that many of the loops are faulted, as is indicated by the stacking fault fringes visible in the larger loops (arrowed B) in this image. A Burgers vector analysis ($\mathbf{g}\cdot\mathbf{b} = 0^*$) performed on the loops has shown them to be Frank partial dislocation loops with $\mathbf{b}$ = 1/3 <111>.

Evidence for helium bubbles on, or in close proximity to, dislocation loops can be seen in Figure 12. In this image several helium bubbles, measuring 1-2 nm in diameter, have been arrowed. Rarely were helium bubbles found within the matrix that were not associated with dislocation loops or dislocations. This observation suggests that either the bubbles nucleated on pre-existing loops or the loops were formed as the bubbles grew in size. Although heterogeneous nucleation of bubbles on the loops cannot be completely ruled out, given that dislocation loops were not visible in the as-received material, before or after welding; and given that only one bubble was ever seen on or near a loop, strongly suggests that the loops were "punched-out" by the growth of helium bubbles. The formation of interstitial dislocation loops by the growth of helium bubbles has been observed by, e.g., Thomas [5] in ion-implanted gold and by Evans et al. [6] in molybdenum and has been treated theoretically by Greenwood et al. [7], Evans [8,9] and most recently by Wolfer [10]. An increase in bubble volume is believed to cause plastic deformation of the adjacent lattice and the subsequent formation of an interstitial dislocation loop.

To further substantiate the hypothesis that these loops were formed by the growth of helium bubbles, an attempt was made to determine if the loops were the interstitial or vacancy type. (Frank loops can be formed by either the precipitation of interstitial atoms or the condensation of vacancies.) This analysis was performed with the methods described by Mazey et al. [11] and Edmunson and Williamson [12], where knowing the inclination of a dislocation loop with

---

* The vector $\mathbf{g}$ corresponds to the reflection giving rise to the image contrast and $\mathbf{b}$ is the Burgers vector of the loops. When $\mathbf{g}\cdot\mathbf{b}= 0$ the loops are invisible in the image.

Close examination revealed that helium bubbles had nucleated on the grain boundaries and the incoherent twin boundaries. The first of these observations is illustrated in Figure 7, a bright field micrograph showing a small section of a grain boundary. As can be seen in this micrograph, the boundary has served as a nucleation site for both carbides (arrowed A) and helium bubbles (e.g., arrowed B). The bubbles in this region averaged ~2.5 nm in diameter and were spaced ~14 nm apart*. It is also interesting to note that helium bubble nucleation was restricted to the boundary plane and the incoherent carbide/matrix interface (carbide interface adjacent to the boundary plane) and not at the coherent or semi-coherent carbide/matrix interface (e.g., arrowed at C). Both the carbide and bubble distributions illustrated in Figure 7 were typical of other grain boundaries at 3.5 mm from the overlay.

As mentioned above, helium bubbles also nucleated on the incoherent twin boundaries. The bubble size and spacing on the boundary segment shown in Figure 8 were approximately 2 nm and 20 nm, respectively. (This boundary was inclined to the electron beam and, as such, the bubble spacing measurement is slightly more accurate than that measured in Figure 7.) The dark contrast along this boundary was caused by the presence of 15 nm diameter carbides that had nucleated on the boundary. A centered-dark field micrograph from this same area (Figure 9) better illustrates the carbide distribution.

Coherent twin boundaries were observed throughout this specimen material. Bubbles were not observed on this boundary type. This observation is illustrated in Figure 10, a micrograph of a coherent twin boundary. In this image, the boundary (marked with an arrow) is tilted with respect to the electron beam. Several bubbles are visible in this micrograph and appear to be associated with the boundary. Tilting experiments, however, showed that these bubbles had actually nucleated on dislocations located adjacent to the boundary plane.

Unlike the as-received specimens, the grain interiors of this material contained a high number density of dislocation loops. The dislocation loops varied in size from 5 to 35 nm in diameter and had

---

* The boundary plane of this segment is nearly normal to the electron beam so that the bubble spacing measured from this micrograph is only a crude estimate of the actual, through-thickness spacing.

[e.g.,13]. Since grain boundaries and incoherent twin boundaries can behave as vacancy sinks, it is possible that during the tritium-charging and aging of the test specimens that vacancy depleted regions developed at these boundary types. As a result, ^3He born in the near boundary region was not trapped as effectively as it is in the grain interiors where the vacancy concentration was much higher, leaving a zone near the boundary essentially free of bubbles except for those that formed on dislocations.

Since coherent twin boundaries are not vacancy sinks, the vacancy argument could explain why large BFZs were observed only at grain boundaries and incoherent twin boundaries in this specimen material. However, as previously mentioned, in many cases there was a slight decrease in bubble density near the coherent twin boundaries. A decrease in bubble density was observed mostly at boundaries that were characterized by having a significant number of dislocations and dislocation pile-ups intersecting the boundary plane. Since dislocations can also act as vacancy sinks it is possible that these small BFZs were also a result of narrow vacancy depleted regions created by the dislocations and not the coherent boundaries themselves.

The nucleation of bubbles on dislocations was also observed within the austenite matrix. Figure 15 is a bright field micrograph illustrating this phenomenon. Here several bubbles (dark imaging in this over-focused image) appear to have nucleated on a dislocation (diffuse background contrast near bubbles). Further examples of dislocation nucleation are shown in Figure 16. In this image, dislocations are located in a large BFZ adjacent to a grain boundary. It appears that the dislocations have "pulled" away from the line of bubbles. This phenomenon was frequently observed in the welded specimens and suggests that it may be a result of recovery processes and/or stress effects that occurred during the overlay process. An additional observation is that bubbles on dislocations appeared to be slightly larger than those associated with the loops.

Helium-bearing Plate (147 appm He, 2.3 mm Below Overlay)

To determine the effect of the weld overlay process on the ^3He bubble distribution, attempts were initiated to section material as near to the weld as possible. The section taken from 2.3 mm below the weld represents this material. (One additional slice was made

respect to the electron beam and the sign of $(\mathbf{g}\cdot\mathbf{b})\mathbf{s}^*$ provides the necessary information for an unambiguous determination. Upon changing the sign of **s**, the image contrast changes from either outside to inside the dislocation core or vice versa depending on the type of loop being imaged and its inclination to the electron beam. This analysis consistently showed that the Frank loops observed in this material were interstitial in nature.

A random distribution of dislocation loops occurred throughout the grain volumes except in the immediate vicinity of the grain boundaries. A denuded zone, free of dislocation loops and essentially free of visible helium bubbles, existed at all grain boundaries and incoherent twin boundaries. These denuded regions have been termed bubble-free zones (BFZs). Figure 13 is an image taken of a region adjacent to an incoherent twin boundary. Only a few dislocation loops have formed within the ~0.6 μm zone nearest to the boundary. Closer examination also revealed this region to be free of additional helium bubbles except for a small number of bubbles that had nucleated on dislocations lying within the denuded region. It should be noted that bubbles smaller than those imaged may have been present in the BFZs but were not visible due to the limitations of the imaging technique.

Additional examples of BFZs are shown in Figure 14. This bright field micrograph was taken from a region of a foil containing a grain boundary (arrowed A) an incoherent twin boundary step (arrowed B) and two coherent twin boundary segments (arrowed C and D). This micrograph shows that BFZs exist at both the grain boundary and the incoherent twin step. In contrast, there is not a BFZ adjacent to the coherent twin boundary segment, C. (A BFZ exists at the coherent segment D but only because of the overlaping BFZs associated with the grain boundary and incoherent twin step.) A closer examination of the image in Figure 14 reveals that, although a BFZ does not exist at boundary segment C, the bubble (loop) density does decrease in the near boundary region. This observation was characteristic of the bubble distribution at many of the coherent twin boundaries in this material.

The reason for the formation of BFZs is not completely understood; however, it may be related to the vacancy concentration in the near boundary regions. Vacancies are known to be strong traps for ^3He

---

* The vector **s** is the deviation from exact diffracting conditions

grain boundaries. Bubbles on this boundary segment measured ~3 nm in diameter and were spaced, on average, 16 nm apart. The bubble distribution on an incoherent twin boundary is illustrated in Figure 20 and the bubble distribution within the interior of the austenite grains is shown in Figure 21.

A bright field image of a coherent twin boundary is shown in Figure 22. As can be seen, there is a significant BFZ adjacent to this boundary. This phenomenon was observed at all coherent twin boundaries (in addition to the grain boundaires and incoherent twin boundaries) in the unwelded 147 appm ^{3}He material and was the only noticable difference in bubble distribution between this material and that which contained a weld. In this image, the shape of the BFZ appears to be dictated by the dislocation distribution and density in the near-boundary region. Also, in areas where the dislocation density is low there are more loops (i.e., bubbles). Conversely, in areas were the dislocation density is high few loops are observed. Further evidence of dislocation/dislocation loop relationship is shown in Figure 23 where a BFZ is observed immediately adjacent to a coherent twin boundary and a dislocation pile-up. These observations may again indicate that dislocations served as vacancy sinks that prevented helium bubbles from nucleating "homogeneously" in the near-boundary regions.

The existence of BFZs at the coherent twin boundaries in the unwelded material and the absence thereof in material containing a weld (compare Figure 22 to Figure 14 - segment, C) implies that welding can "heal" the denuded regions. This may occur because the increased vacancy concentration at the welding temperatures could allow for the nucleation of additional helium bubbles and the subsequent formation of dislocation loops in these regions. Also, the movement or annilation of dislocations that had initially served as nucleation sites for helium bubbles could give rise to bubbles within the BFZ.

Helium Bubble Distributions

The results of the bubble size and spacing measurements for the specimens examined are summarized in Tables 2 and 3. Reference to these tables shows that there were no significant differences in bubble size and spacing between the specimen material that did and did not contain a weld. Bubble spacing in Table 3 is expressed as visible bubble spacing and loop spacing. Visible bubbles were those

closer to the weld but during specimen preparation this material cracked extensively and the specimens could not be completed.) The microstructure of this slice was very similar to that observed in the 3.5 mm slice, consisting of large, 150 - 200 μm austenite grains containing a low number density of dislocations. Additionally, carbides were usually observed on the high angle grain boundaries. The helium bubble distribution was also comparable to that described at 3.5 mm below the weld overlay. Figure 17 is a bright field micrograph from this specimen material that illustrates the helium bubble distribution on the grain boundaries. The bubble size and bubble spacing measured from this image yielded a diameter of ~3 nm and a spacing of ~15 nm. The bubble distribution in the grain interiors is shown in Figure 18. In this image, helium bubbles are again associated with dislocation loops. As in the 3.5 mm material, the bubble diameter was ~2 nm.

BFZs were also observed in this specimen material. Similar to the 3.5 mm material, large, ~0.5 μm BFZs were observed adjacent to the grain boundaries. No significant BFZs were observed at the coherent twin boundaries but, as in the 3.5 mm material, in some cases a slight decrease in the loop density was observed in the near-boundary region. No incoherent twin boundaries could be located within these TEM foils and hence the bubble distributions adjacent to this boundary type is unknown.

Helium-bearing Plate (147 appm He, No Weld)

It is known that the tritium-charging, aging and offgassing steps employed by Sandia National Laboratories will result in formation of helium bubble microstructures [14]. Therefore, to further characterize the effects of the weld overlay process on the helium bubble distribution, and to determine the extent of the bubble distribution that existed prior to welding, material containing 147 appm ^{3}He that had not experienced a weld overlay was examined in the TEM.

The base microstructure of this specimen material was consistent with that observed for other 147 appm ^{3}He specimens described above. Observations also showed that a well-developed bubble microstructure did exist in this material. The bubble distribution is evident in representative images (Figures 19 - 21) from this material. Figure 19 illustrates the helium bubble distribution at the

ACKNOWLEDGEMENTS

The authors wish to gratefully acknowledge F. E. Odom, E. E. Kemper and A. W. Lacey for their able assistance during the course of this research program. The authors would also like to express their gratitude to Dr. M. R. Louthan, Jr. for many useful discussions.

REFERENCES

1. W. R. Kanne, Jr., Welding Journal, Vol. 67, 1988, pp. 33-39.

2. A. K. Birchenall and E. A. Franco-Ferreira, "Progress Report - Welding for Reactor Vessel Repair", SRL Memorandum, DPST-89-255, January 23, 1989.

3. W. R. Kanne, Jr., D. A. Lohmeier, K. A. Dunn, and M. H. Tosten, Microstructural Science, Vol. 19, in press.

4. M. F. Rhüle: in Radiation-Induced Voids in Metals, Proc. Int. Conf. Radiation-Induced Voids in Metals, June 1971, J. W. Corbett and L. C. Ianniello, eds., U. S. Atomic Energy Commission, 1972, pp. 255-91.

5. G. J. Thomas, Rad. Effects, Vol. 78, 1983, pp. 37-51.

6. J. H. Evans, A. Van Veen and L. M. Caspers, Rad. Effects, Vol. 78, 1983, pp. 105-120.

7. G. W. Greenwood, A. J. E. Foreman and D. E. Rimmer, J. Nucl. Matls., Vol. 4, pp. 305-324.

8. J. H. Evans, J. Nucl. Mater., Vol. 68, 1977, pp. 129-140.

9. J. H. Evans, J. Nucl. Mater., Vols. 76 and 77, 1978, pp. 228-234.

10. W. G. Wolfer, Phil. Mag. A, Vol. 58, 1988, pp. 285-297.

11. D. J. Mazey and R. S. Barnes and A. Howie, Phil. Mag., Vol. 7, 1962, pp. 1861-70.

12. B. Edmondson and G. K. Williams, Phil. Mag., Vol. 9, 1964, pp. 227-283.

actually observed within the matrix - adjacent to the dislocation loops. In some cases, however, bubbles could not be imaged at some of the loops, presumably, because they were too small. Given this, the actual bubble spacing is then more accurately expressed as loop spacing. The results of these measurements have also shown that there was no change in bubble size and spacing at distances greater than 2.3 mm below the weld overlay for the weld parameters and ^3He concentration employed in this study.

CONCLUSIONS

The results have shown that the low heat input GMA technique produces limited changes in microstructure and helium bubble distribution as compared to the unwelded material. Plastic strain produced by the overlay process was estimated at no more than 2-3% at distances as close as 1 mm and much less at 3 mm from an overlay. A well-developed bubble microstructure was observed in the base material prior to welding, a result of the tritium charging and aging procedure. Bubbles were observed within the austenite matrix, on dislocations and on grain boundaries and incoherent twin grain boundaries. Bubbles in the matrix were commonly associated with the Frank-type interstitial dislocation loops. The results have also shown that there were no significant differences in bubble microstructure (size and spacing) between the unwelded material and the material with a weld at distances 2.3 mm or greater below the GMA weld overlays. BFZs were observed in all specimen material at the grain boundaries and the incoherent twin boundaries. In the material that did not contain a GMA overlay, BFZs were also observed at the coherent twin boundaries. Finally, the overlay process appears to "heal" BFZs at the coherent twin boundaries.

FUTURE WORK

Currently research is underway to examine the bubble distribution in the near weld region of specimen material containing 48.5 appm ^3He. This will help provide a more complete picture of the bubble distributions that develop immediately below the weld overlays.

TABLE 1. ALLOY COMPOSITION (wgt. %)

Cr	Ni	Mn	Si	C	P	S	Fe
18.22	8.28	1.39	0.52	0.073	0.023	0.016	Bal

13. E. V. Kornelsen and A. A. van Gorkum, J. Nucl. Mater. Vol. 92, 1980, pp. 79-88.

14. S. H. Goods, Private communication, 1990.

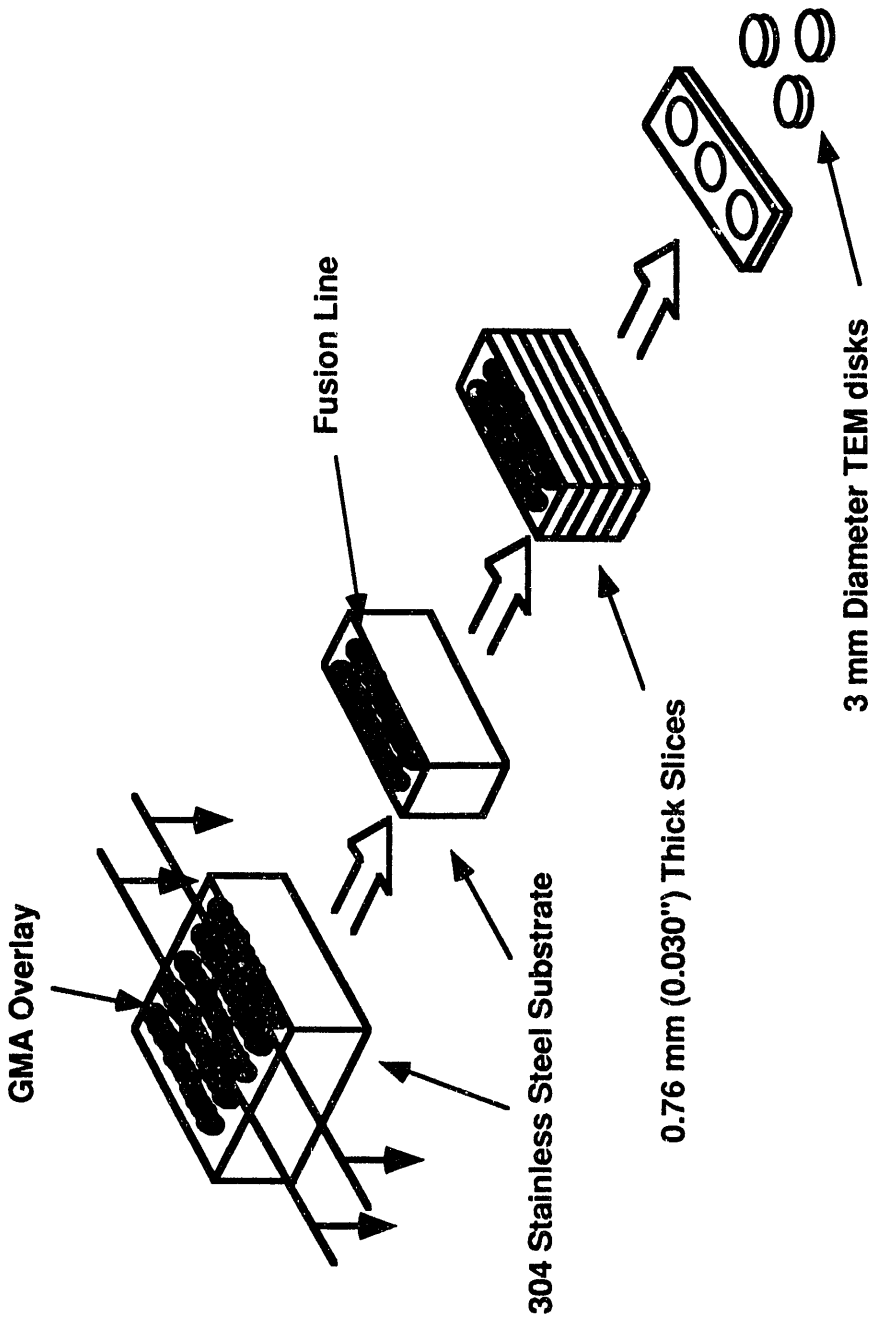

Figure 1. A diagram that illustrates the steps required to prepare 3 mm diameter TEM disks from the substrate material. The base plate containing a weld was sliced parallel to the fusion line, thinned to ~0.1 mm and punched into 3 mm diameter disks.

TABLE 2. BUBBLE SIZE (nm)

	Matrix	GB+	ICTB†
No Weld	2	4	2
Slice 1*	2	2-3	?
Slice 2**	2	2-3	2

* 2.3 mm below weld overlay
* * 3.5 mm below weld overlay.
\+ Grain Boundaries (High Angle)
† Incoherent Twin Boundaries

TABLE 3. BUBBLE SPACING (nm)

	Boundaries		Matrix	
	GB+	ICTB†	Loops	Visible
No Weld	20	21	50-130	135
Slice 1*	16	?	20-120	115
Slice 2**	13	25	20-110	120

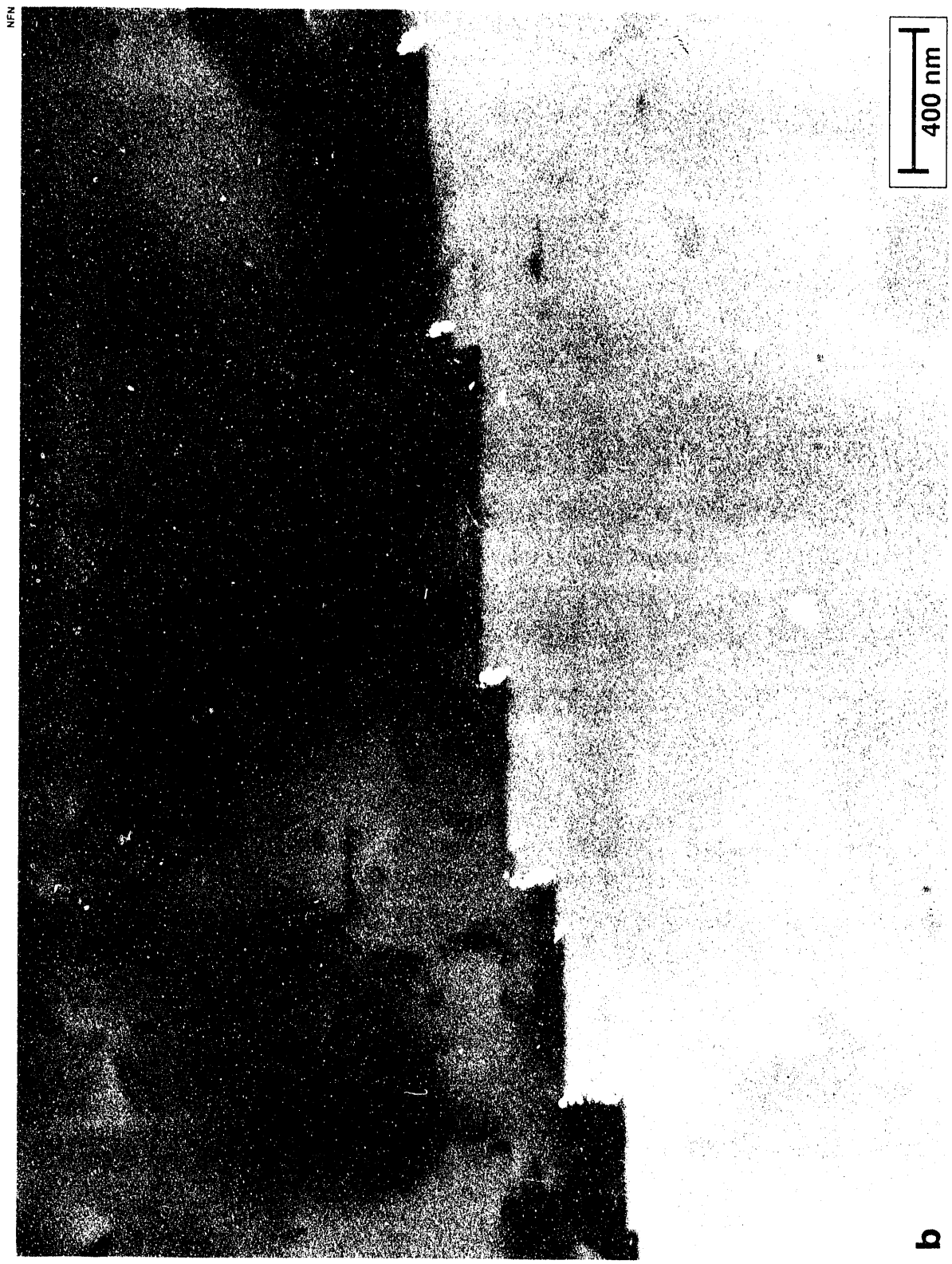

Figure 2b. As-received material (no weld). Centered-dark field image of carbides on the incoherent steps shown in Figure 2a.

Figure 2a. As-received material (no weld). Bright field micrograph of incoherent twin boundary steps.

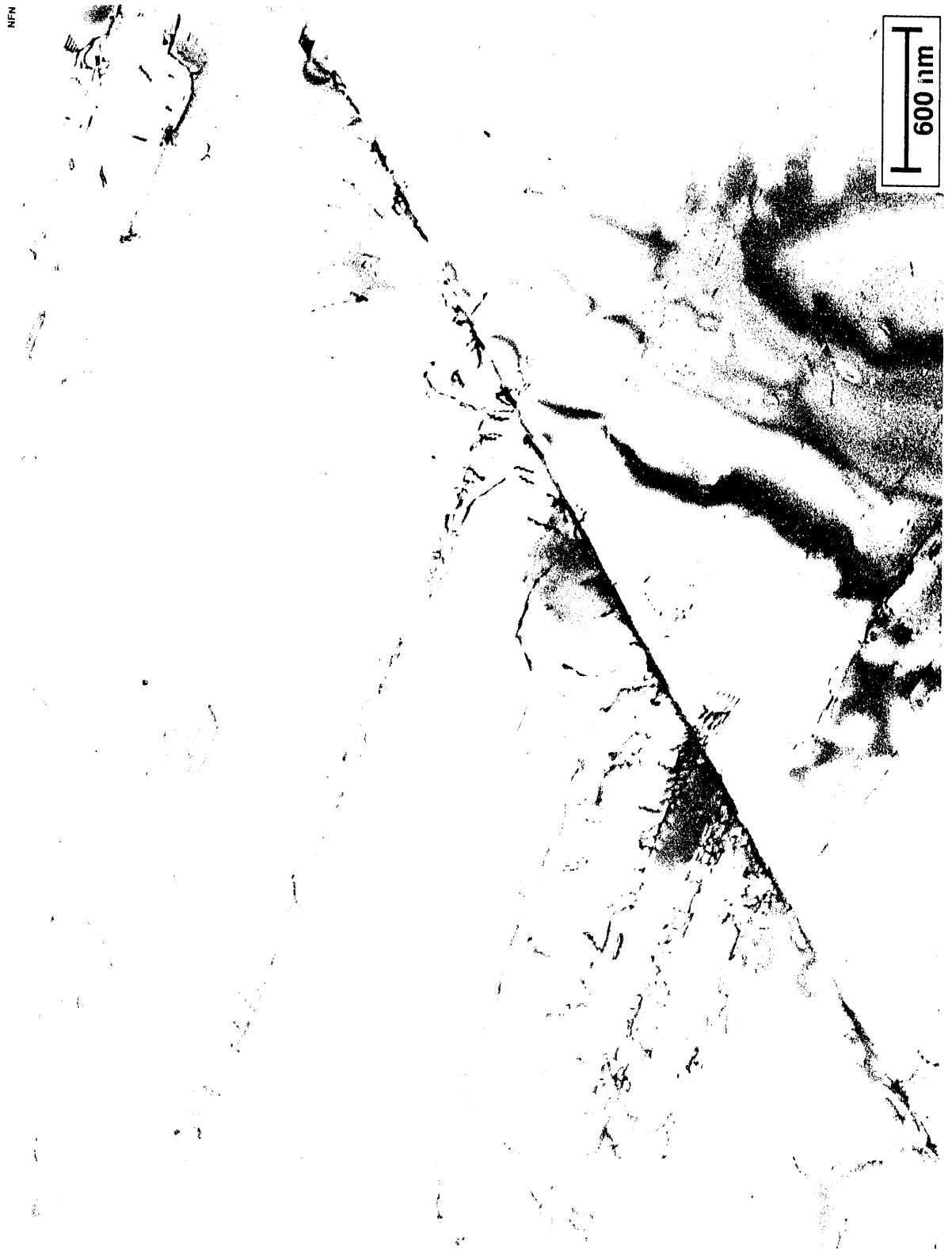

Figure 4. As-received plate with weld overlay. Dislocation pile-ups intersecting a coherent twin boundary ~3 mm below the weld.

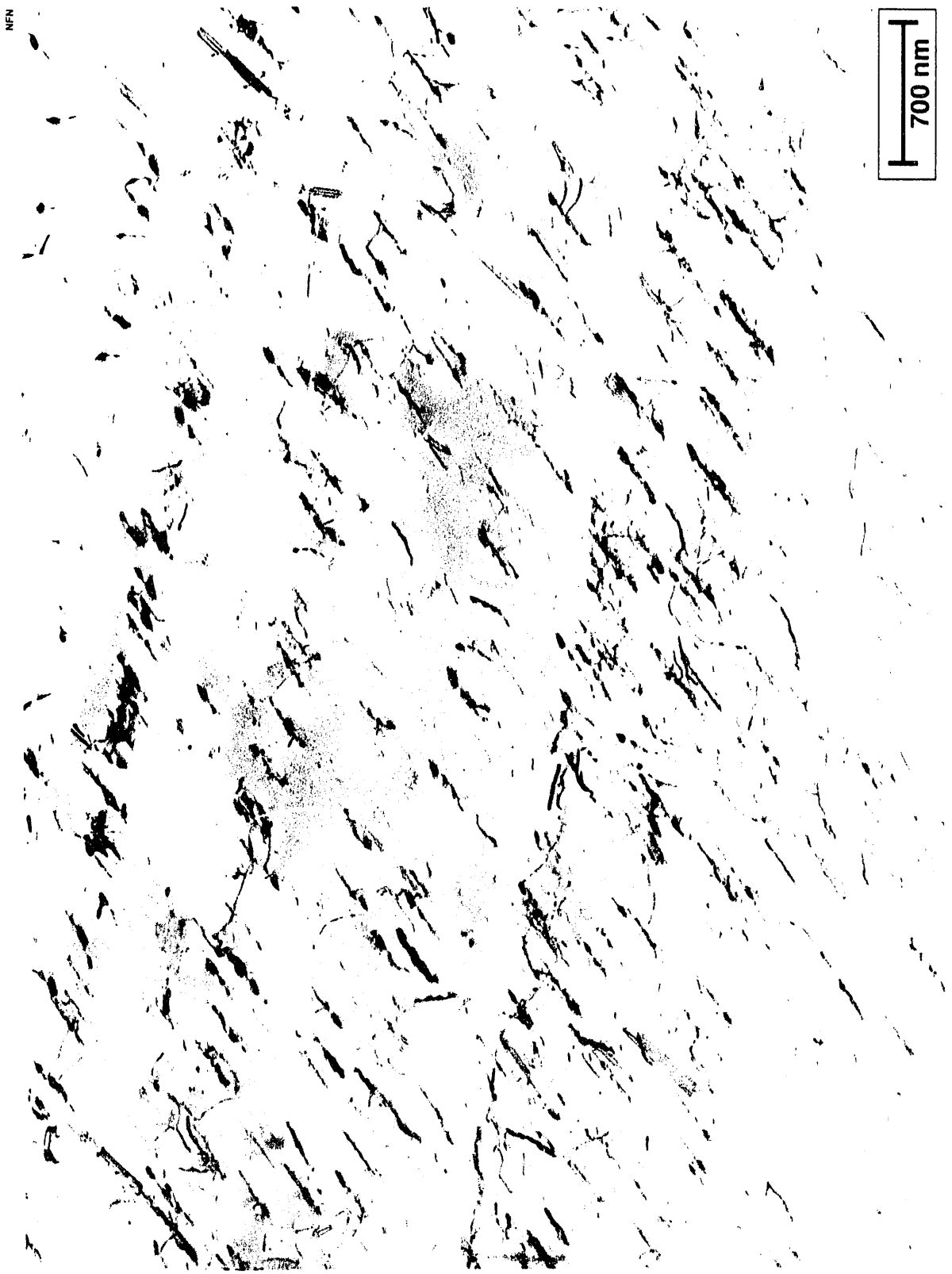

Figure 3. As-received plate with weld overlay. Planar dislocation arrays at 3 mm below the weld.

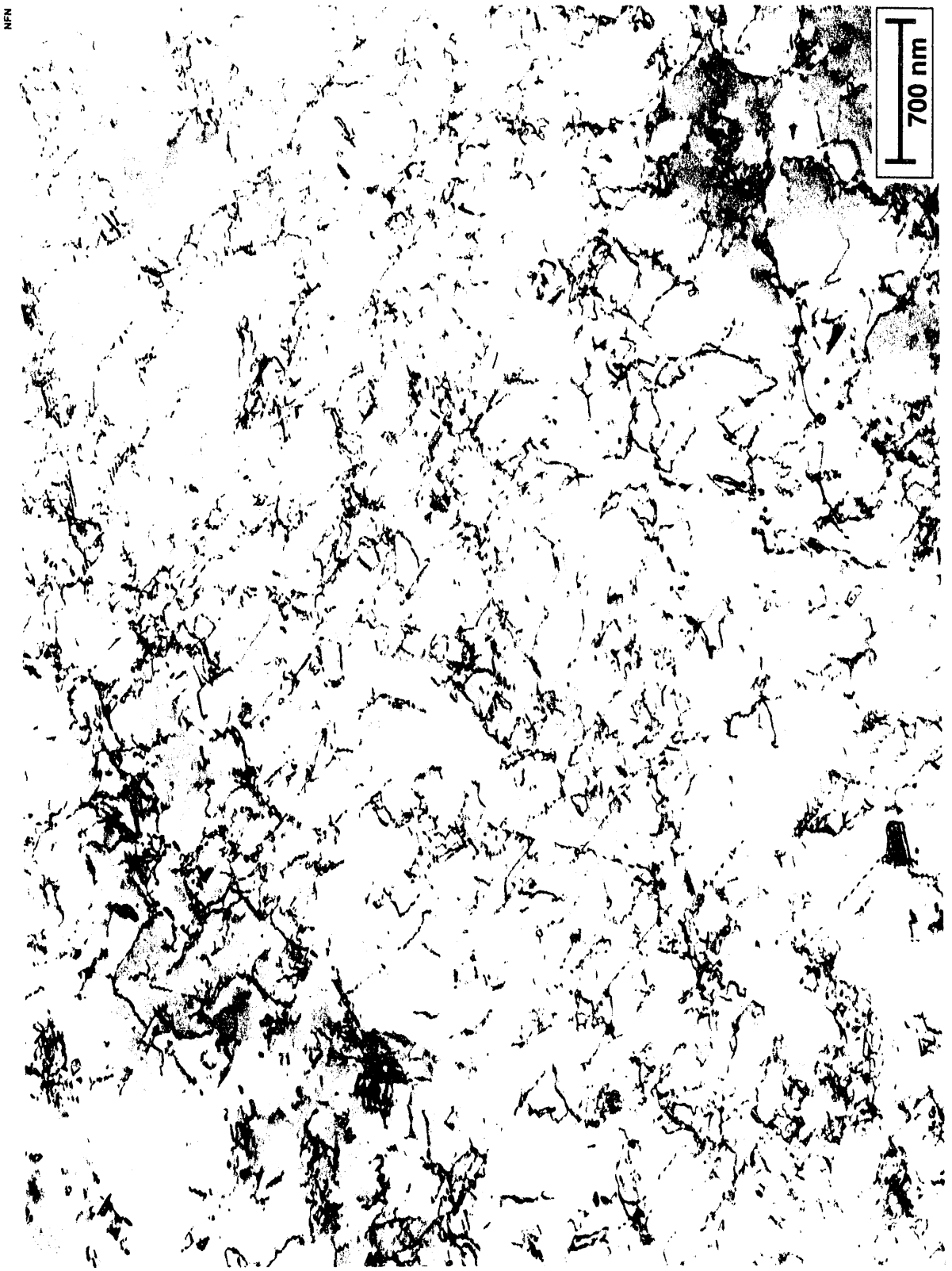

Figure 6. As-received material with a weld overlay. Dislocation substructure observed at ~1 mm below the weld. Note the absence of planar dislocation arrays in this area.

Figure 5. As-received plate with weld overlay. Increased dislocation density in the vicinity of a coherent twin boundary at ~1 mm below an overlay.

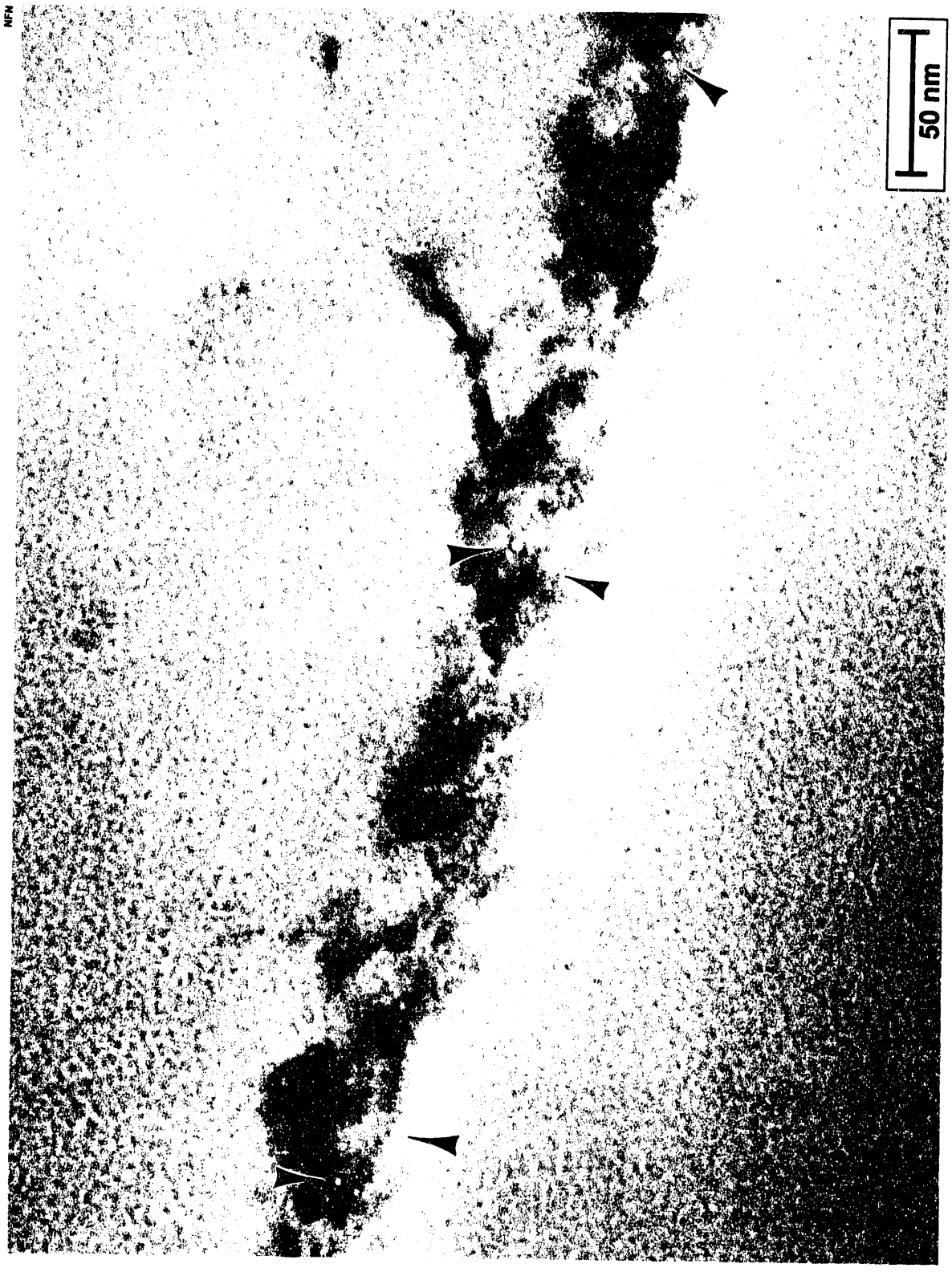

Figure 8. Helium-bearing plate (3.5 mm below weld overlay). Helium bubble distribution on an incoherent twin boundary. Several He bubbles have been arrowed. The dark contrast on the boundary is caused by the presence of a large number of small carbides.

Figure 7. Helium-bearing plate (3.5 mm below weld overlay). Carbide particles (at A) and helium bubbles (e.g., at B) on a grain boundary. Bubbles are not observed at the carbide/matrix interface (at C).

Figure 10. Helium-bearing plate (3.5 mm below weld overlay). Coherent twin boundary (arrowed) is inclined to the electron beam. Bubbles visible in this micrograph are associated with matrix dislocations.

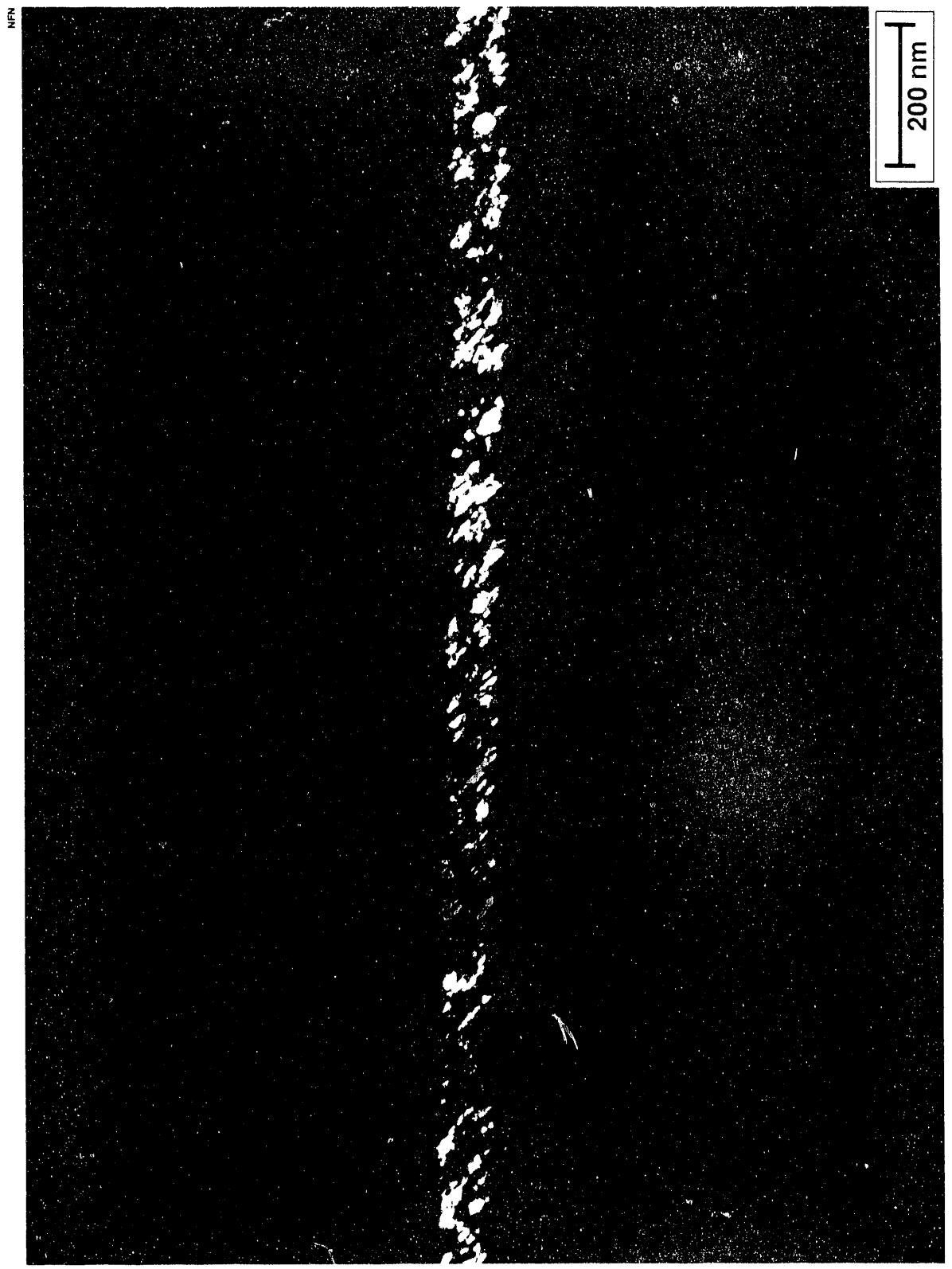

Figure 9. Helium-bearing plate (3.5 mm below weld overlay). Centered-dark field micrograph of carbides on the boundary shown in Figure 8.

Figure 12. Helium-bearing plate (3.5 mm below weld overlay). Helium bubbles (at arrows) associated with dislocation loops.

Figure 11. Helium-bearing plate (3.5 mm below weld overlay). Typical dislocation loop distribution found within the grain interiors.

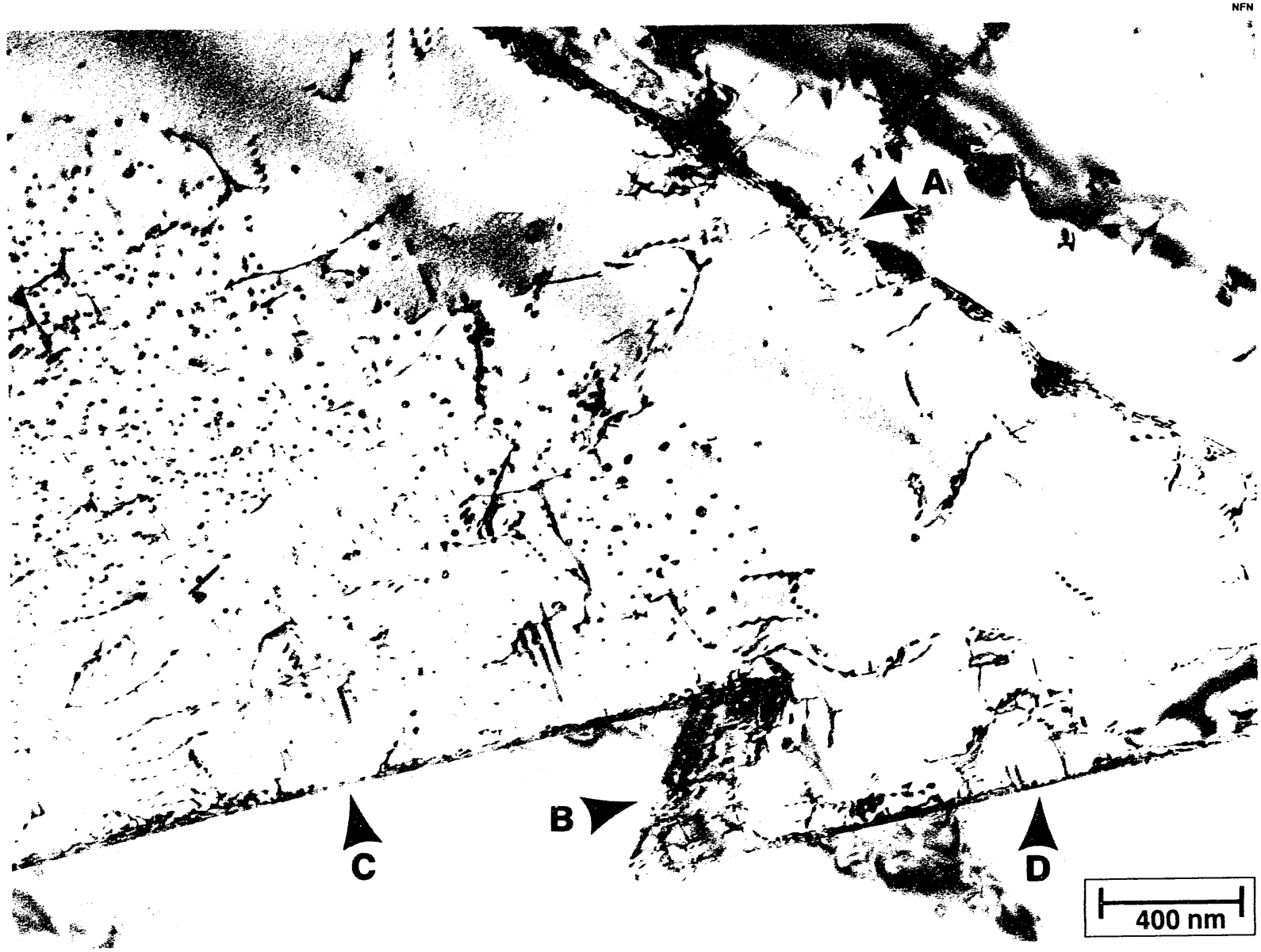

Figure 14. Helium-bearing plate (3.5 mm below weld overlay). Bubble-free zones adjacent to a grain boundary (at A) and an incoherent twin boundary step (at B). Coherent twin boundary segments are labeled C and D.

Figure 13. Helium-bearing plate (3.5 mm below weld overlay). Bubble-free zone adjacent to an incoherent twin boundary.

Figure 16. Helium-bearing plate (3.5 mm below weld overlay). Helium bubbles associated with dislocations within a bubble-free zone. Dislocations (at arrows) appear to have moved away from the line of helium bubbles.

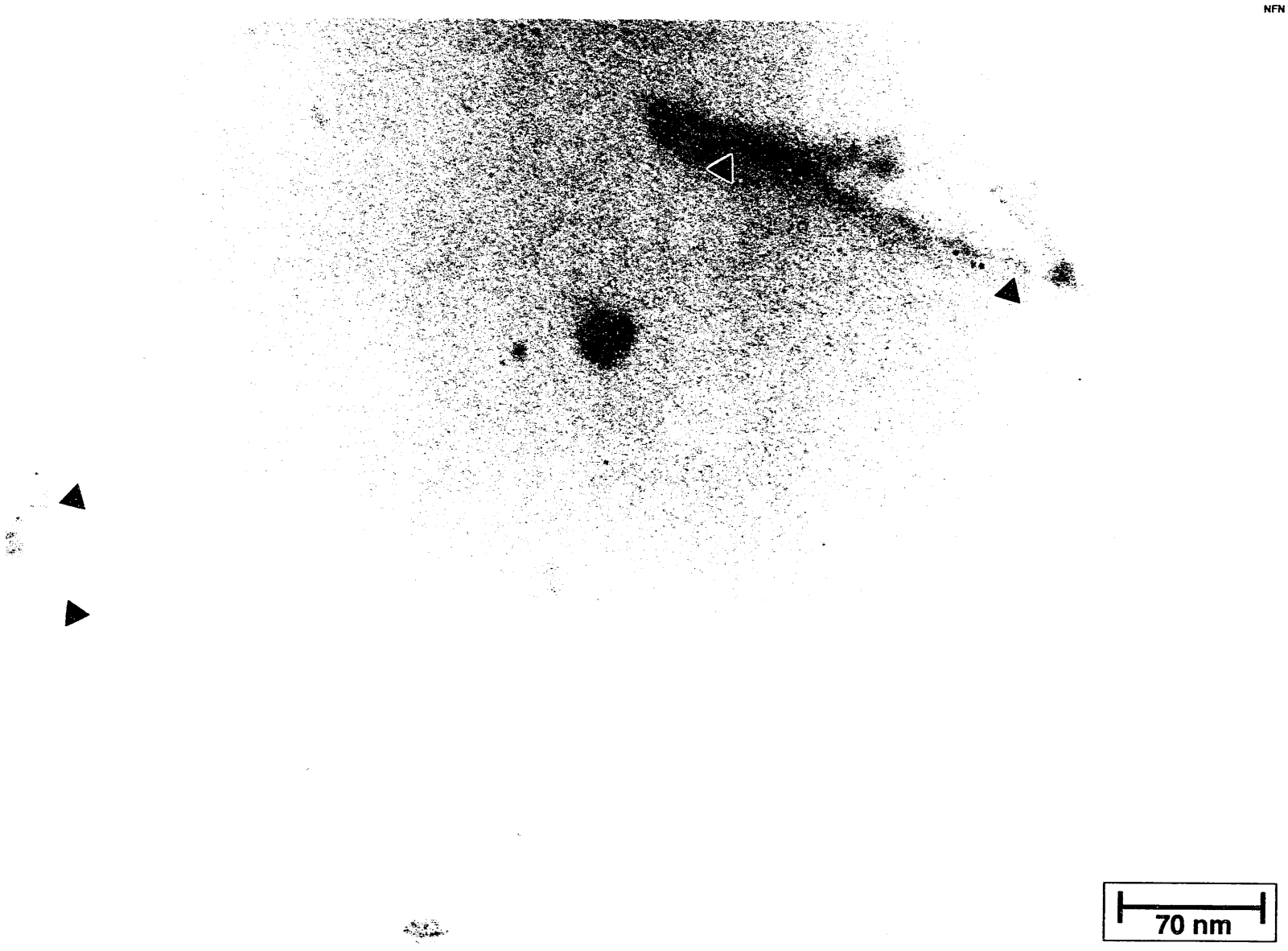

Figure 15. Helium-bearing plate (3.5 mm below weld overlay). An over-focused image of helium bubbles (dark imaging) that have nucleated on dislocations (at arrows).

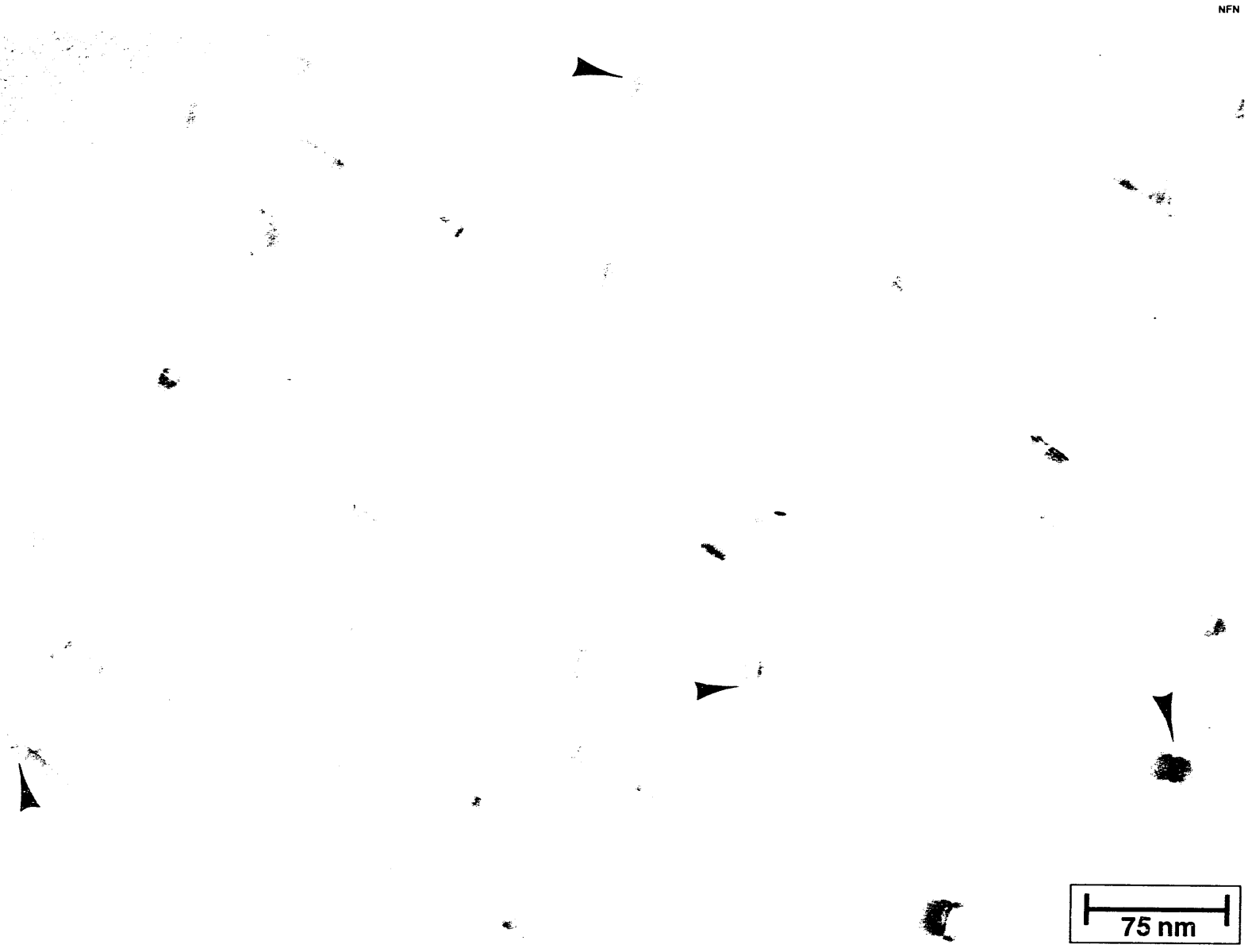

Figure 18. Helium-bearing plate (2.3 mm below weld overlay). Typical helium bubble and dislocation loop distribution within a grain interior. Arrows mark the location of several helium bubbles.

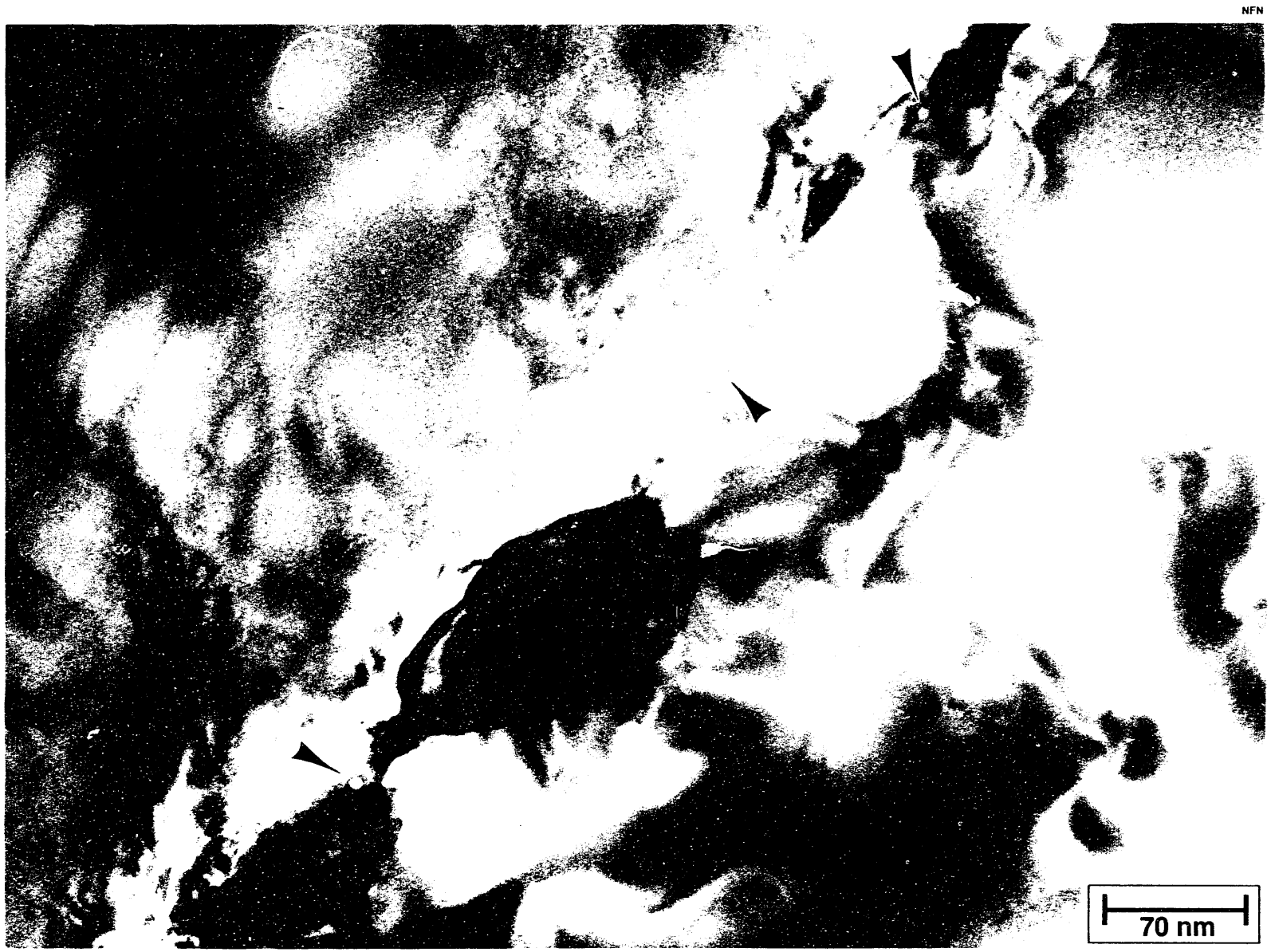

Figure 17. Helium-bearing plate (2.3 mm below weld overlay). Helium bubble distribution on a grain boundary. Several large bubbles have been arrowed. The dark particles on the boundary are carbide precipitates.

Figure 20. Helium-bearing plate (no weld overlay). Typical helium bubble distribution on an incoherent twin boundary. Several helium bubbles have been arrowed.

Figure 19. Helium-bearing plate (no weld overlay). Helium bubble distribution on a grain boundary. Several carbides are also located on this boundary.

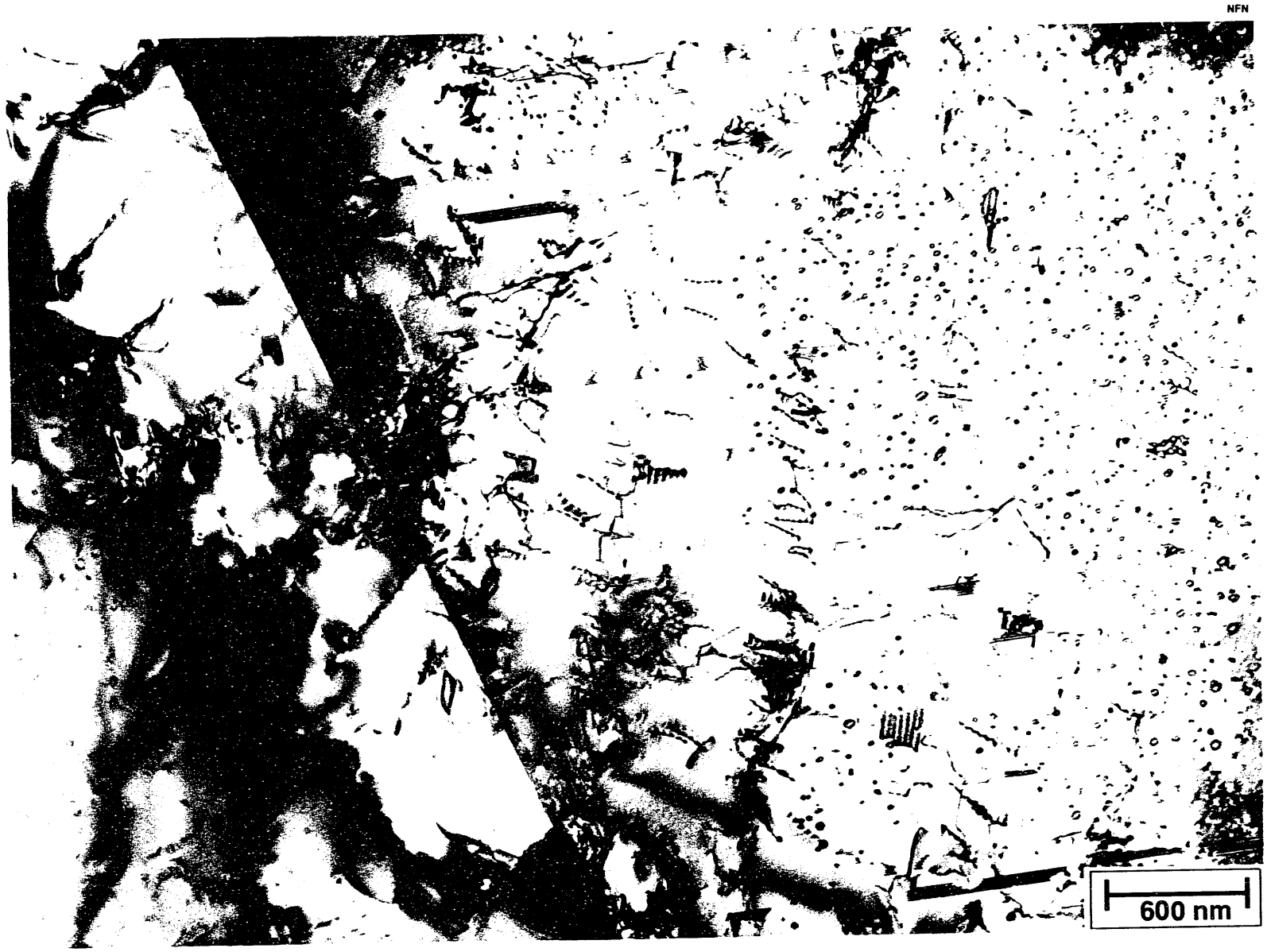

Figure 22. Helium-bearing plate (no weld overlay). Bubble-free zone adjacent to a coherent twin boundary.

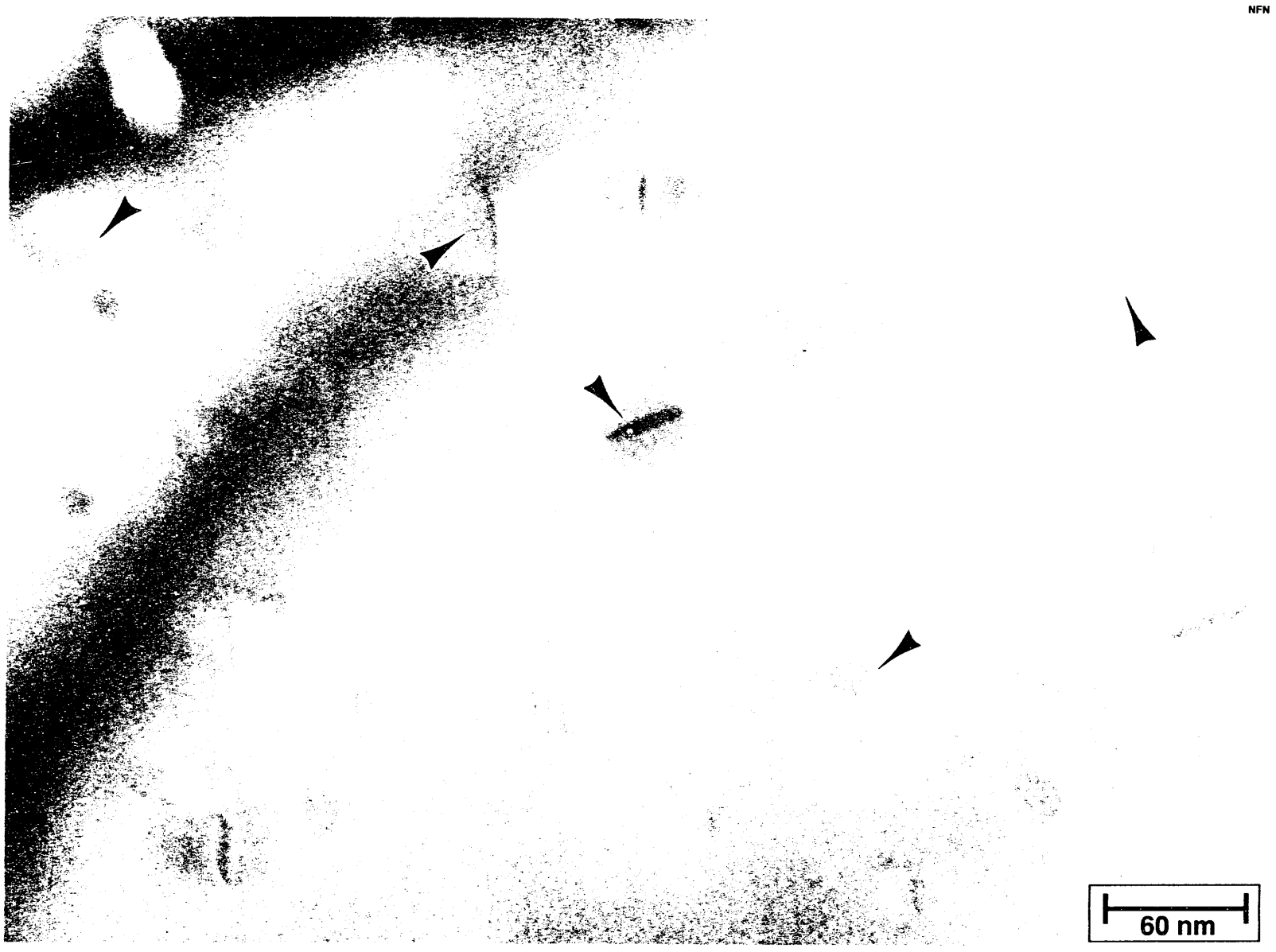

Figure 21. Helium-bearing plate (no weld overlay). Helium bubbles and dislocation loops within a grain interior. Arrows indicate location of bubbles.

Figure 23. Helium-bearing plate (no weld overlay). Bubble-free zone at a coherent twin boundary (arrowed) and a dislocation pile-up.

DATE
FILMED
2 15 93